Acta Oceanol. Sin., 2017, Vol. 36, No. 5, P. 105–114
DOI: 10.1007/s13131-017-1065-4
http://www.hyxb.org.cn
E-mail: hyxbe@263.net

The polarimetric features of oil spills in full polarimetric synthetic aperture radar images

ZHENG Honglei[1], ZHANG Yanmin[1]*, WANG Yunhua[1], ZHANG Xi[2], MENG Junmin[2]

[1] College of Information Science and Engineering, Ocean University of China, Qingdao 266100, China

[2] The First Institute of Oceanography, State Oceanic Administration, Qingdao 266061, China

Received 15 October 2016; accepted 2 December 2016

Abstract

Compared with single-polarized synthetic aperture radar (SAR) images, full polarimetric SAR images contain not only geometrical and backward scattering characteristics, but also the polarization features of the scattering targets. Therefore, the polarimetric SAR has more advantages for oil spill detection on the sea surface. As a crucial step in the oil spill detection, a feature extraction directly influences the accuracy of oil spill discrimination. The polarimetric features of sea oil spills, such as polarimetric entropy, average scatter angle, in the full polarimetric SAR images are analyzed firstly. And a new polarimetric parameter P which reflects the proportion between Bragg and specular scattering signals is proposed. In order to investigate the capability of the polarimetric features for observing an oil spill, systematic comparisons and analyses of the multipolarization features are provided on the basis of the full polarimetric SAR images acquired by SIR-C/X-SAR and Radarsat-2. The experiment results show that in C-band SAR images the oil spills can be detected more easily than in L-band SAR images under low to moderate wind speed conditions. Moreover, it also finds that the new polarimetric parameter is sensitive to the sea surface scattering mechanisms. And the experiment results demonstrate that the new polarimetric parameter and pedestal height perform better than other polarimetric parameters for the oil spill detection in the C-band SAR images.

Key words: full polarimetric synthetic aperture radar, oil spill detection, multipolarization features

Citation: Zheng Honglei, Zhang Yanmin, Wang Yunhua, Zhang Xi, Meng Junmin. 2017. The polarimetric features of oil spills in full polarimetric synthetic aperture radar images. Acta Oceanologica Sinica, 36(5): 105–114, doi: 10.1007/s13131-017-1065-4

1 Introduction

Oil pollution in the ocean environment is a matter of great concern because of the threats generated by such pollution to marine operations and wildlife. There is a great effort by scientists around the world on developing surveillance systems that can efficiently detect and monitor oil spills in the ocean environment. The synthetic aperture radar (SAR) is an active, coherent, band-limited microwave high-resolution sensor that provides valuable measurements at both day and night. Moreover, the SAR is almost independent of atmospheric conditions. The SAR has been proven to be a valuable tool for the detection of sea oil pollution, under low to moderate wind conditions (Nunziata et al., 2013; Solberg et al., 2007). The scattering mechanisms occur on a slick covered surface is different from which occur on a clean sea surface. For the clean sea surface, the echo signals are mainly dominated by Bragg scattering for incident angles from about 20°–70°. When the sea surface is covered by oil spill, the short gravity and capillary waves are damped, and this damping effect is responsible for the reduction of the backscattered microwave signals. Therefore, oil spills can be observed as "dark pitches" in the SAR images (Fiscella et al., 2000; Migliaccio et al., 2015; Migliaccio and Tranfaglia, 2005; Zhang et al., 2011). And thus the SAR is considered as an effective instrument to detect oil spills on the sea surface.

Generally, oil spill detection can be divided into three steps: (1) dark area detection, (2) feature extraction, and (3) oil spill/look-alike classification (Brekke and Solberg, 2005; Solberg et al., 2007). The second step, i.e., the feature extraction is important to the accuracy of classification. Conventional single-polarization SAR intensity images have been employed for sea oil slick observation purpose. Compared with a single-polarized SAR, a full-polarized SAR yields more useful information and can acquire four channels polarimetric data, i.e., hh, hv, vh and vv. Then, there is a general consensus that the polarimetric SAR is able to provide additional information for the oil spill detection (Li et al., 2015 ; Migliaccio et al., 2015, 2009; Migliaccio and Tranfaglia, 2005; Salberg et al., 2014; Velotto et al., 2011). In Schuler et al. (2006), Cloude-Pottier decomposition theorem was used to develop ways of detecting and classifying ocean surface features. A polarimetric entropy, anisotropy, and average scatter angle of the Cloude-Pottier decomposition theorem are investigated when slicks are present (Schuler and Lee, 2006). In Migliaccio et al. (2009), the CPD (copolarized phase difference) was used to characterize the scattering return from oil spills and biogenic slicks. Under low to moderate wind conditions, the CPD standard deviation for oil spill is larger, while for biogenic slicks the value of the CPD standard deviation is similar to that for the sea water (Migliaccio et al., 2009). In Nunziata et al. (2011), a pedestal height was also used to investigate oil slicks, and the parameter was proven to be sensitive to the sea surface scattering mech-

Foundation item: The National Natural Science Foundation of China under contract Nos 41576170 and 41376179; the Public Science and Technology Research Funds Projects of Ocean (Ocean University of China) under contract No. 2013418025-2.
*Corresponding author, E-mail: yanminzhang@ouc.edu.cn

anisms. Oil spills can be distinguished from sea background by using the pedestal height (Nunziata et al., 2011). Nunziata et al. (2013) proposed a new way to distinguish oil slicks from sea water based on the use of the degree of polarization. In Skrunes et al. (2014), the magnitude of a copolarization correlation coefficient was applied in oil spill detection, the copolarization correlation coefficient is high for the clean sea areas, whereas in the slick-covered regions the values of the copolarization correlation coefficient are general much smaller. The decreased copolarization correlation coefficient in the slick-covered regions may due to the presence of several scattering mechanisms or a scattering mechanism which is different from the clean surface scattering (Skrunes et al., 2014).

Till now, for a polarimetric SAR oil spill detection, most of the papers focus on oil spill detection by using C-band or L-band SAR. However, few of them discuss the differences between C-band and L-band. Which band is more suitable for oil spill detection? Which polarimetric features are more useful to extract oil slicks from the sea background? To clarify these questions, in this paper, we compare the C-band polarimetric SAR with the L-band. Besides, a new polarimetric parameter that can be used to distinguish oil slicks is also proposed. Moreover, eight polarimetric features at two bands are investigated and discussed. The experiments are conducted on SIR-C/X-SAR and Radarsat-2 data which are collected under low to moderate wind speeds. The remaining of this paper is organized as follows: in Section 2 the theoretical background is reviewed, in Section 3, some meaningful experiments are presented and discussed. The conclusions are drawn in Section 4.

2 Theory

2.1 *The dampen effect caused by slicks*

Oil slicks on the sea surface will dampen the small-scale sea waves, and then the sea surface covered by slick is much smoother than clean sea. The damping effect caused by slicks can be described by the Marangoni theory. According to the Marangoni theory (Lombardini et al., 1989), the spectrum of the sea surface covered by oil films is related to the clean sea surface spectrum by

$$\psi_{\text{oil}}(k) = \frac{\psi_{\text{water}}(k)}{y_{\text{r}}(k)}, \tag{1}$$

where k is the spatial wavenumber of the water wave; $\psi_{\text{oil}}(k)$ denotes the spectrum covered by oil; $\psi_{\text{water}}(k)$ denotes the clean sea surface spectrum and the damping ratio y_{r} (k) caused by slicks is given by

$$y_{\text{r}}(k) = \frac{1}{1 - F + F/y(k)}, \tag{2}$$

where F is the fractional filling factor; $y\,(k)$ can be expressed as

$$y\,(k) = \frac{1 \pm 2\tau \pm 2\tau^2 - X + Y(X + \tau)}{1 \pm 2\tau \pm 2\tau^2 - 2X + 2X^2}, \tag{3}$$

where

$$X = \frac{E_0 k^2}{\rho\sqrt{2\nu\omega^3}}, Y = \frac{E_0 k}{4\nu\rho\omega}, \omega = \sqrt{gk + \frac{\eta k^3}{2\omega}}, \tau = \sqrt{\frac{\omega_{\text{D}}}{2\omega}}. \tag{4}$$

In Eq. (4), $\eta = 74 \times 10^{-3}$ N/m, is the surface tension; $\rho = 10^3$ kg/m^3, is the water density; $g = 9.8$ m/s^2, is the acceleration of gravity; $\nu = 10^{-6}$ m/s^2, is the kinematic viscosity; $E_0 = 9$ mN/m, is the elasticity modulus; and $\omega_{\text{D}} = 6$ rad/s is the characteristic frequency (Pinel et al., 2008). Obviously, the damping ratio $y_{\text{r}}(k)$ is related to the sea wave number.

When microwaves illuminate the sea surface, the scattering fields can be approximately described by two kinds of scattering mechanisms, i.e., Bragg scattering and specular scattering. The backscattered signal intensity of Bragg scattering is much stronger than the specular scattering while the incidence angle ranges from 20° to 70°. The relationship between the Bragg and the electromagnetic wave number is

$$k_{\text{B}} = 2k_{\text{ra}} \sin\theta_{\text{i}}, \tag{5}$$

where k_{ra} is the radar wavenumber; k_{B} is the wavenumber of the Bragg waves; and θ_{i} denotes the incidence angle. In this work, the damping effect caused by slicks for C-band and L-band Bragg sea waves is simulated by Eq. (2). Figure 1 presents the damping effect caused by slicks for Bragg waves corresponding to C- and L-band microwaves. In Fig. 1, the damping ratio increases with the incidence angle at L-band. While for C-band, the maximum damping ratio is located about 30°. For the incidence angle smaller than 30°, the damping ratio increases with the incidence angle. For the incidence angle larger than 30°, the damping ratio decreases with the incidence angle. Overall, the damping ratio for C-band is larger than L-band. The difference of the damping ratio will influence the capacity of oil spill detection at two bands.

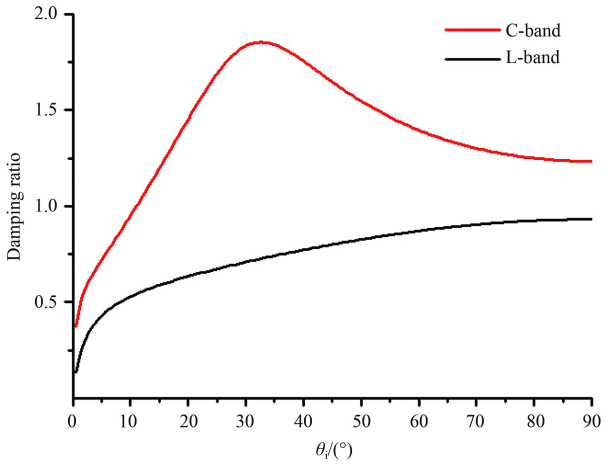

Fig. 1. The damping effect of slick on Bragg sea waves. The red and black lines correspond to C- and L-band, respectively. The damping ratio is log-transformed.

2.2 *Polarimetric features for oil spill observation*

The full polarimetric scattering matrix is given as

$$\boldsymbol{S} = \begin{bmatrix} S_{\text{hh}} & S_{\text{hv}} \\ S_{\text{vh}} & S_{\text{vv}} \end{bmatrix}, \tag{6}$$

and the matrix elements represent the measured complex scattering coefficients. The first and second superscripts refer to the polarizations of the sent and received signals respectively, where h denotes horizontal and v the vertical polarization. From the full polarimetric scattering matrix, the Pauli scattering vector

$\vec{k} = \frac{1}{\sqrt{2}}[S_{hh} + S_{vv} \quad S_{hh} - S_{vv} \quad 2S_{hv}]^T$ can be extracted in which T denotes transpose. Here, the reciprocity condition, i.e., $S_{hv} = S_{vh}$, is used. Then, the 3×3 polarimetric coherency matrix $\boldsymbol{T}_3$ is obtained as

$$\boldsymbol{T}_3 = \vec{k}\vec{k}^{*T}, \tag{7}$$

where the subscript * denotes the complex conjugate. The averaged coherency matrix $\langle \boldsymbol{T}_3 \rangle$ is defined as (Cloude and Pottier, 1996)

$$\langle \boldsymbol{T}_3 \rangle = \frac{1}{N}\sum_{i=1}^{N} \boldsymbol{T}_{3i}. \tag{8}$$

2.2.1 *Polarimetric entropy and average scatter angle*

The coherency matrix can be written in the form:

$$\langle [\boldsymbol{T}_3] \rangle = [\boldsymbol{U}_3][\Sigma][\boldsymbol{U}_3]^{-1} = \sum \lambda_i \vec{u}_i \vec{u}_i^{*T}, \tag{9}$$

where $[\Sigma]$ is a 3×3 diagonal matrix with nonnegative real elements; $[U] = [\ \vec{u}_1 \quad \vec{u}_2 \quad \vec{u}_3\ ]$, is a unitary matrix where $\vec{u}_1$, $\vec{u}_2$ and $\vec{u}_3$ are the three unit orthogonal eigenvectors; and λ_i is the eigenvalue of the 3×3 polarimetric coherency matrix.

The entropy (H) is defined from the logarithmic sum of eigenvalues as

$$H = -\sum_{i=1}^{3} P_i \log_3 P_i, \tag{10}$$

where P_i are the probabilities obtained from the eigenvalues of the 3×3 polarimetric coherency matrix with

$$P_i = \frac{\lambda_i}{\sum_{i=1}^{3} \lambda_i}. \tag{11}$$

In the physical domain, the entropy represents the randomness of scattering mechanisms. If the value of the entropy is small, the system will contain significant polarimetric information.

The eigenvectors of the 3×3 polarimetric coherency matrix is introduced in the form:

$$\vec{\boldsymbol{u}} = \left[\cos\alpha_i, \sin\alpha_i \cos\beta_i e^{i\delta_i}, \sin\alpha_i \sin\beta_i e^{i\gamma_i}\right]^T, \tag{12}$$

where α_i is the scattering parameter that represents an internal degree of freedom of the scatterer; β_i is the orientation of the scatterer about the radar line of sight; and δ_i and γ_i are phase shifts between the different polarization-dependent components. The average scattering angle α can be expressed as

$$\alpha = P_1\alpha_1 + P_2\alpha_2 + P_3\alpha_3. \tag{13}$$

The value of average scattering angle is related to the scattering mechanism. Compared with the surrounding clean ocean, the oil film can effectively smooth the ocean surface and change the root-mean-square (RMS) slope. Therefore, the scatter angles of slicks are different with the clean sea.

2.2.2 *Pedestal height*

Durden et al. (1990) put forward a pedestal height (h_p) as the ratio of minimum eigenvalue to maximum eigenvalue (Lee and Pottier, 2009):

$$h_p = \frac{\min(\lambda_1, \lambda_2, \lambda_3)}{\max(\lambda_1, \lambda_2, \lambda_3)} = \frac{\lambda_3}{\lambda_1}. \tag{14}$$

As a measure of the unpolarized backscattered energy, the pedestal height is expected to be low in the case of an oil-free sea surface, and much larger in the case of an oil-covered sea surface. Accordingly, the pedestal height is expected to be able to distinguish oil spills from the sea backgrounds.

2.2.3 *Standard deviation of copolarized phase difference*

The standard deviation of the CPD is the standard deviation (d_s) of a copolarized phase difference and it can be expressed as

$$d_s = \sqrt{\left\langle (\phi_{hh} - \phi_{vv})^2 \right\rangle - (\langle \phi_{hh} - \phi_{vv} \rangle)^2}. \tag{15}$$

For Bragg scattering, the phase difference between the measured complex scattering coefficients S_{hh} and S_{vv} is (almost) 0°. For slick surface, the phase difference between two copolarized channels, however, is obviously larger. According to Schuler et al. (1993), the CPD is small in the case of Bragg resonant backscatter from a slightly rough ocean surface. Hence, the increase in d_s, i.e., the broadening of the phase distribution, which is observed in the slick areas, may be caused by a specular scattering.

2.2.4 *Co-polarization correlation coefficient*

The magnitude of the correlation coefficient (r) is expressed as

$$r = \frac{|\langle S_{hh} S_{vv}^* \rangle|}{\sqrt{\langle |S_{hh}|^2 \rangle \langle |S_{vv}|^2 \rangle}}, \tag{16}$$

where r is sensitive to the characteristic of the target on the sea surface. The lower value of the correlation coefficient implies depolarization effect. For the sea surface Bragg scattering mechanism, vv-polarized echoes are highly correlated with hh-polarized echoes. While non-Bragg scattering mechanism is expected to call for the low correlation between vv- and hh-polarized echoes.

2.2.5 *Degree of polarization*

The degree of polarization (d_p) can be defined in terms of Mueller matrix:

$$d_p = \sqrt{\frac{1}{3}\left(\frac{\mathrm{tr}(\boldsymbol{M}^T\boldsymbol{M})}{\boldsymbol{M}_{11}^2} - 1\right)}, \tag{17}$$

where $\boldsymbol{M}$ is the 4×4 Mueller matrix. For more details, please see Nunziata et al. (2013). When dealing with the sea water surface without oil, Bragg scattering is expected to call for low depolarization, and the value of d_p is close to 1. When the oil slick is present, non-Bragg scattering mechanism is expected to call for high depolarization, and the value of the d_p is close to 0. The value of the d_p shows a completely different sensitivity with respective oil-covered and oil-free sea surfaces.

2.2.6 *Copolarization power ratio*

A copolarization power ratio can be expressed as

$$\gamma = \frac{\left\langle |S_{\rm hh}|^2 \right\rangle}{\left\langle |S_{\rm vv}|^2 \right\rangle}. \tag{18}$$

According to the basic scattering theory of the ocean surface, the measured complex scattering coefficients $S_{\rm hh}$ and $S_{\rm vv}$ can be represented as

$$S_{\rm hh} = S_{\rm hh}^{\rm sp} + S_{\rm hh}^{\rm B}, \tag{19}$$

$$S_{\rm vv} = S_{\rm vv}^{\rm sp} + S_{\rm vv}^{\rm B}, \tag{20}$$

where the subscripts refer to two kinds of scattering mechanisms and the superscripts sp denotes the specular scattering and B denotes Bragg scattering. The copolarization power ratio of water can be expressed as

$$\gamma_{\rm wa} = \frac{\left\langle \left| S_{\rm hh}^{\rm B} + S_{\rm hh}^{\rm sp} \right|^2 \right\rangle}{\left\langle \left| S_{\rm vv}^{\rm B} + S_{\rm vv}^{\rm sp} \right|^2 \right\rangle}. \tag{21}$$

According to a SPM (small perturbation method), the first-order scattering coefficient caused by Bragg scattering can be written as

$$\sigma_{pp}^0(\theta_i) = 16\pi k_{\rm ra}^4 \cos^4\theta_i \left| g_{pp} \right|^2 \psi(k, \phi_{\rm B}), \tag{22}$$

where $\psi(k, \phi_{\rm B})$ denotes a sea surface spectrum. $\phi_{\rm B}$ is the azimuthal angle between a radar-look direction and the wind direction; pp denotes hh or vv; and g_{pp} is a geometric factor. Moreover, the relationship between the first-order scattering coefficient σ_{pp}^0 and the measured complex scattering codfficient $S_{pp}^{\rm B}$ is

$$\sigma_{pp}^0 = 4\pi \left| S_{pp}^{\rm B} \right|^2. \tag{23}$$

Combining Eqs (1), (21), (22) and (23), the copolarization power ratio of slick ($\gamma_{\rm sl}$) can be expressed as

$$\gamma_{\rm sl} = \frac{\left\langle \left| S_{\rm hh,wa}^{\rm B} / \sqrt{y_{\rm r}(k)} + S_{\rm hh,wa}^{\rm sp} \right|^2 \right\rangle}{\left\langle \left| S_{\rm vv,wa}^{\rm B} / \sqrt{y_{\rm r}(k)} + S_{\rm vv,wa}^{\rm sp} \right|^2 \right\rangle}, \tag{24}$$

where the subscript wa (water) denotes the scattering from the oil-free surface. According to the SPM theory, we know that vv-polarized channel presents a stronger echo signal, i.e., $S_{\rm vv}^{\rm B} > S_{\rm hh}^{\rm B}$. Moreover, as discussed in Section 2, the values of the damping ratio $y_{\rm r}(k)$ are generally larger than 1. The microwave echo of the specular scattering is much weaker than Bragg scattering when the incidence angle is larger than 30°. Thus, oil spill has a larger copolarization power ratio value than sea water.

2.2.7 *Polarimetric parameter*

In the present work, a new polarimetric parameter P can be defined as

$$P = \frac{\left\langle |S_{\rm hh} + S_{\rm vv}|^2 \right\rangle}{\left\langle |S_{\rm hh} - S_{\rm vv}|^2 \right\rangle}. \tag{25}$$

According to the Bragg scattering mechanism, the phase difference between the measured complex scattering coefficients $S_{\rm hh}^{\rm B}$ and $S_{\rm vv}^{\rm B}$ is (almost) 0 for sea water, and we may model the elements of the scattering matrix (Salberg et al., 2012) as

$$\begin{bmatrix} S_{\rm hh}^{\rm B} \\ S_{\rm vv}^{\rm B} \end{bmatrix} = \begin{bmatrix} \alpha_{\rm hh,\ vv} & 1 \\ 1 & 0 \end{bmatrix} \begin{bmatrix} S_{\rm vv}^{\rm B} \\ n \end{bmatrix} \tag{26}$$

where n is a random scalar introduced to model the random difference between $S_{\rm hh}^{\rm B}$ and $S_{\rm vv}^{\rm B}$. The scalar $\alpha_{\rm hh,\ vv}$ denotes the amplitude ratio between the vertical and horizontal polarizations. The relationships between $S_{\rm vv}^{\rm B}$ and $S_{\rm hh}^{\rm B}$, $S_{\rm vv}^{\rm sp}$ and $S_{\rm hh}^{\rm sp}$ are as follows

$$S_{\rm hh}^{\rm B} = \alpha_{\rm hh,\ vv} S_{\rm vv}^{\rm B} + n, \tag{27}$$

$$S_{\rm hh}^{\rm sp} = -S_{\rm vv}^{\rm sp}. \tag{28}$$

Using Eqs (19), (20) and (25)–(28), the new parameter P is derived as

$$P \approx \frac{\left\langle \left| (\alpha_{\rm hh,\ vv} + 1) S_{\rm vv}^{\rm B} \right|^2 \right\rangle}{\left\langle \left| (\alpha_{\rm hh,\ vv} - 1) S_{\rm vv}^{\rm B} - 2 S_{\rm vv}^{\rm sp} \right|^2 \right\rangle} = \frac{1}{\dfrac{\left\langle \left| \alpha_{\rm hh,\ vv} - 1 \right|^2 \right\rangle}{\left\langle \left| \alpha_{\rm hh,\ vv} + 1 \right|^2 \right\rangle} + \dfrac{4 \left\langle \left| S_{\rm vv}^{\rm sp} \right|^2 \right\rangle}{\left\langle \left| (\alpha_{\rm hh,\ vv} + 1) S_{\rm vv}^{\rm B} \right|^2 \right\rangle}}. \tag{29}$$

In the derivation of Eq. (29), we have supposed that the measured complex scattering coefficients $S_{\rm vv}^{\rm B}$ and $S_{\rm vv}^{\rm sp}$ are uncorrelated with each other, i.e., $S_{\rm vv}^{\rm B} S_{\rm vv}^{\rm sp*} = 0$. Under low to moderate conditions, the electromagnetic scattering processes of sea surface can be modeled as two kinds of mechanisms, i.e., Bragg scattering and the specular scattering. For the incidence angle ranging from 20° to 70°, Bragg scattering mechanism generally plays a leading role and the specular scattering only accounts for a smaller proportion for the oil-free surface (Skrunes et al., 2012), which leads to a smaller value of $4 \left\langle \left| S_{\rm vv}^{\rm sp} \right|^2 \right\rangle / \left\langle \left| (\alpha_{\rm hh,\ vv} + 1) S_{\rm vv}^{\rm B} \right|^2 \right\rangle$, a larger value of the new parameter P. Once an oil spill presents, the surface becomes smoother because the short gravity and capillary waves are damped. In this case, the specular scattering accounts for a larger proportion, the factor $4 \left\langle \left| S_{\rm vv}^{\rm sp} \right|^2 \right\rangle / \left\langle \left| (\alpha_{\rm hh,\ vv} + 1) S_{\rm vv}^{\rm B} \right|^2 \right\rangle$ becomes larger. As a consequence, the value of the new parameter in the slicks is expected to be smaller. Thus, one can classify a SAR image with oil slicks in it into different classes rely on the value of the new parameter. It is important to note the new parameter is available under low to moderate wind speeds. If the wind speed is large enough, sea waves will be broken. As a result, the scattering processes will be more complex. The new parameter would be ineffective to distinguish an oil slick.

3 Experiments

3.1 *Comparison of poalrimetric features at C-band and L-band*

According to the results simulated in Fig. 1, the oil slick seems to have a greater impact on Bragg sea waves at C-band. In order to verify this conclusion, six SIR-C/X-SAR images at C-band and

L-band are processed in this part. The SIR-C/X-SAR imaging radar took its first flight on the space shuttle endeavour in April 1994 and flew for a second time in October 1994. This multifrequency radar has fully polarimetric capability at C- and L-band, and a single polarization at X-band (X-SAR). The incidence angle of the radar ranges from 20° to 55° and the SAR swath width on the ground varies between 15 and 90 km. During the missions STS-59 (April 1994) and STS-68 (September and October 1994), C-band and L-band full polarimetic data were acquired at same time. Therefore, we can compare C-band SAR data with L-band in despite of the other environmental factors. More details are summarized in Table 1 (Migliaccio et al., 2009).

Table 1. C- and L-band SIR-C/X SAR dataset

Processing number	Type and band	Time of acquisition	Wind speed/m·s^{-1}	Incidence angle/(°)
PR17040	MLC L	1994-04-11 10:49	low to moderate	35.5–40.4
PR17041	MLC C	1994-04-11 10:49	low to moderate	35.5–40.4
PR44326	MLC L	1994-10-01 08:14	low to moderate	44.1–47.5
PR44327	MLC C	1994-10-01 08:14	low to moderate	44.1–47.5
PR49938	MLC L	1994-10-08 05:57	4.0	47.2–49.9
PR49939	MLC C	1994-10-08 05:57	4.0	47.2–49.9

All of the images listed in Table 1 were acquired under low to moderate wind speeds. Among the three groups data, the first group data are presented and discussed in detail, similar conclusion can be drawn from the other two groups.

Figure 2 shows the vv polarization images of PR17041 (C-band) and PR17040 (L-band), which are acquired under low to moderate conditions. The incidence angle varies from 35.5°–40.4°. The dark areas related to the slicks are visible both in C- and L-band vv polarization images. The color bars indicate the value of the NRCS (normalized radar cross section).

The value of the NRCS is plotted in Fig. 3 based on the two white lines in Fig. 2, which are related to two different bands. For hh polarized channel (Fig. 3a), the NRCS of sea water is about –23 dB for C-band and L-band. And the NRCS of the slick is about –27 dB at L-band while the value is about –32 dB at C-band. Obviously, C-band (9 dB) has a high contrast than L-band (4 dB) between the slick and the sea water. For vv polarized channel (Fig. 3b), the NRCS values of the sea water at C- and L-band are also similar to each other, and the values are both about –18 dB. The signal value of the slick is –23 dB for L-band, –28 dB for C-band. A higher NRCS contrast between the slick and the sea water can also be observed at C-band. The results in Fig. 3 show that the intensity of the echoes backscattered from sea water at C-band is similar to L-band. However, the intensity of the echoes backscattered from the slicks present an obvious difference between C- and L-band polarized channels. Knowing from Fig. 1, the oil film performs a heavy damping effect for C band Bragg waves and induces a weaker backscattered intensity. As a consequence, the oil spills are more significant in C-band SAR images.

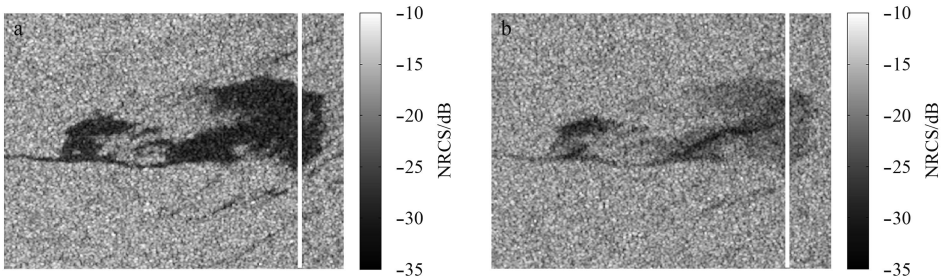

Fig. 2. NRCS of vv polarized channel. a. C-band and b. L-band.

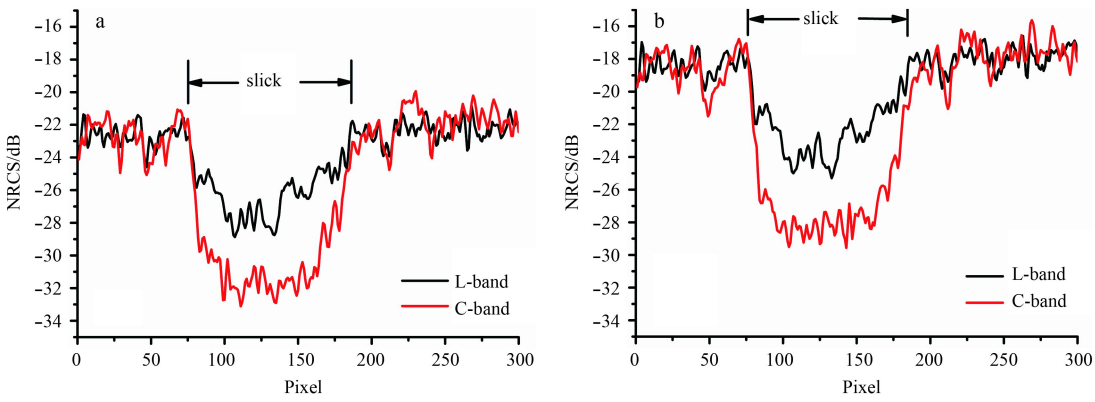

Fig. 3. The NRCS of vv polarized channel at C-band and L-band. The red and black lines correspond to the transection in C-band (see Fig. 2a) and L-band images (see Fig. 2b). a. hh polarized channel and b. vv polarized channel.

Figures 4a–h show the eight multipolarization features at C-band and L-band. From Fig. 4, the slick is clearly distinguished from the sea background in the eight polarization feature images at C-band. However, the oil slick cannot be easily identified by a visual inspection at L-band polarimetric features images. When the radar wave illuminates on the sea surface, the scatter mech-

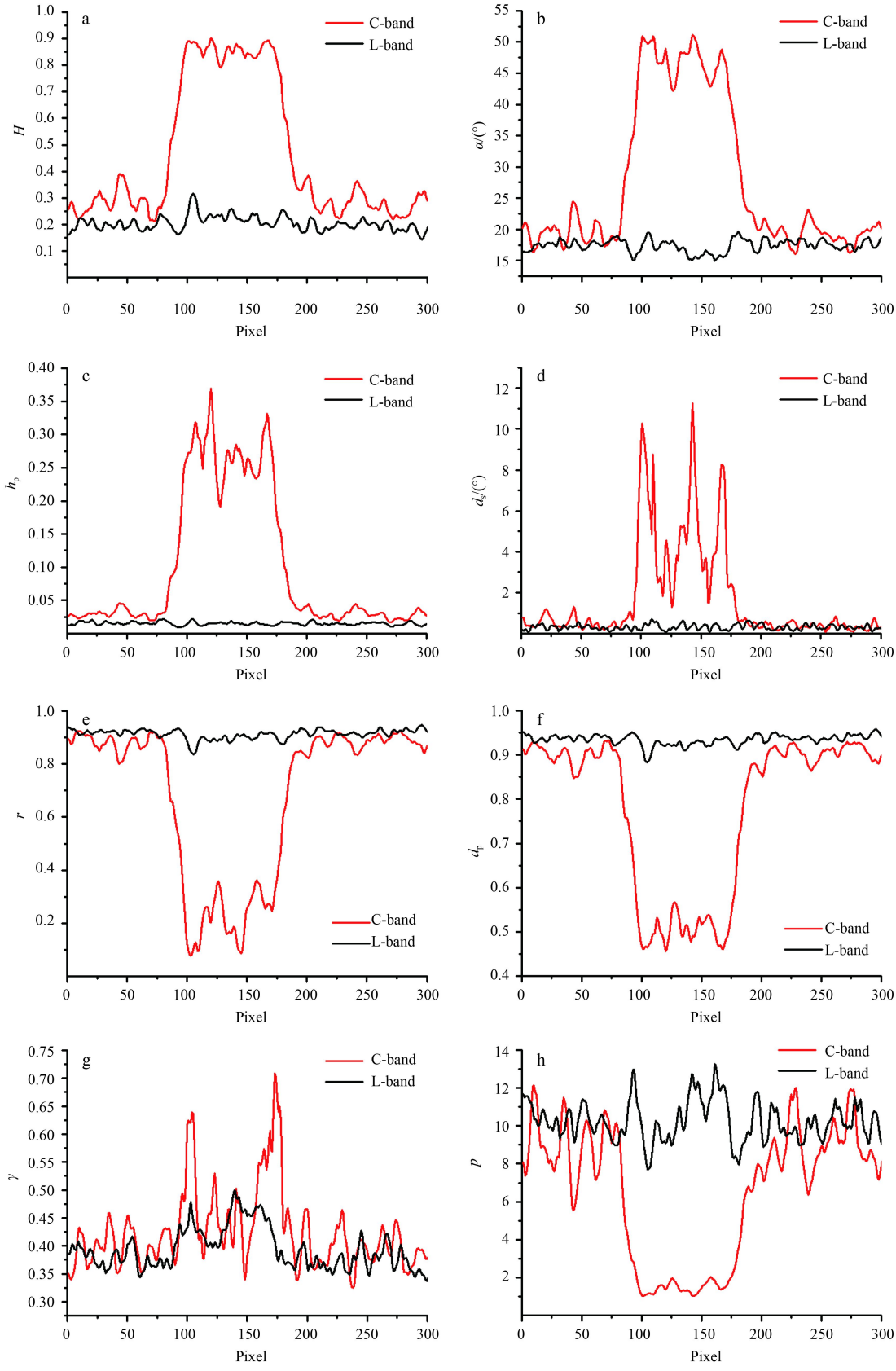

Fig. 4. Polarimetric features in C-band and L-band images. The red and black lines denote the transection in Figs 2a and b, respectively.

anisms of the slicks and the sea water are differ from each other. Many efforts have been made to explain the scattering processes. Generally speaking, under low to moderate conditions, Bragg scattering dominates for the slick-free surface. Bragg scattering is expected to call for a low depolarization. When a slick is present, non-Bragg scattering is in place. This scattering mechanism is expected to call for a high depolarization. In Fig. 4a, the polarimetric entropy of the oil spill is higher than 0.8 while the value of sea water is lower than 0.4 at C-band. However, both slicks and sea water are characterized as a lower polarimetric entropy property at L-band. This phenomenon means that the polarimetric entropy at L-band cannot accurately indicate that the randomness of scattering mechanisms occurs on the oil spill surface. Figure 4b shows the mean scattering angle (α) which is a descriptor of different scattering mechanisms. If the value of the mean scattering angle is below 30°, the surface Bragg scattering is dominant. If the value of it is between 30° and 50°, a dipole scatter is dominant, and if it is between 50° and 90°, an even-bounce scatter is dominant. In Fig. 4b, for C-band, the value of the mean scattering angle for the oil slick is larger than 40°, which suggests a non-Bragg scattering is dominant. However, for the clean sea surface, the value of the mean scattering angle is smaller than 30°, and this suggests that the scattering field is dominated by the surface Bragg scattering. By comparisons, the value of the mean scattering angle for L-band is smaller than 20° in the oil covered area. And thus, it is impossible to discriminate the slicks from the sea backgrounds by a mean scatter angle in L-band SAR images. Figure 4c shows the pedestal height of the ROIs. As a measurement of depolarized backscattered energy, the pedestal height is expected to be high in the oil-covered areas. In Fig. 4c, it is clear that the value in the oil spill region is higher than the oil-free sea at C-band. However, there is no significant difference between the oil-covered and the oil-free areas in L-band SAR image.

The polarimetric entropy, mean scatter angle and pedestal height extracted by using the C-band full poalrimetric SAR data can better reflect the scattering mechanisms. Similar conclusions can be drawn from other features, e.g., the standard deviation of the copolarized phase difference, the co-polarization correlation coefficient, the degree of polarization. While for the copolarization power ratio, the parameter performs not as well as other features mentioned above at C-band. But compared with L-band, the C-band copolarization power ratio is somewhat better on discriminating oil spills.

In fact, the scattering mechanisms occur on the oil-free and oil-covered surfaces are complex processes. We try to explain the processes in terms of two kinds of scatter mechanisms, i.e., Bragg scattering mechanism and the specular scattering mechanism. For the sea surface, the scatter field is dominated by Bragg scattering under low to moderate wind conditions if the incidence angle ranges from 20° to 70°. When oil is spilled on the sea surface, it will spread to form a thin layer on the water surface. This layer will dampen gravity-capillary waves on the ocean surface. The roughness of sea surface covered with oil is much smaller than the clean sea surface. In this case, the specular scatter accounts for a larger proportion among the whole scatter process. The scatter process occurred on the slick surface become more complex. The parameter P described in Section 2 could measure the proportion of the specular scatter mechanism. Figure 4h presents the parameter P extracted from Fig. 2. For C-band, the parameter values of the oil-covered water are quite small because the specular scattering mechanism accounts for a larger proportion. The oil-free area has a larger parameter value than the oil contaminant area because Bragg scattering mechanism accounts for a major proportion. The parameter P is sensitive to the sea surface scattering mechanisms. It is proven that the parameter P is also a useful feature to observe an oil slick at C-band.

3.2 *Classification based on polarimetric features*

On the basis of the above experiments, one can notice that C-band the full polarimetric SAR performs better than L-band under the same conditions. To further compare the two bands, we conduct a segment method to the eight features. Here, due to space constraints, only the segment results by the parameter P are discussed in detail. A threshold method is used to separate the oil slicks from sea water. First, the PDF (probability distribution function) of the polarimetric features for the oil-free areas (the pixels in rectangles in Fig. 5) is established. We assume that the sea water within a narrow incidence angle has a constant polarimetric feature value and that the distribution is only due to speckle. Then, the minimum values of pixels in the rectangles are regarded as thresholds. In Fig. 6a, the red solid line denotes the PDF of the whole region presented in Fig. 5a, the black solid line denotes the PDF of the pixels in the rectangles. The dashed line denotes the minimum values of pixels in the rectangles which are set as thresholds.

The example histograms in Fig. 6 are evaluated based on the polarimetric parameter P. The black curves represent the values of the clean sea surface, and the red lines include all pixels in the polarimetric parameter P images, i.e., values from both the oil-free area and the oil-covered area. In Fig. 6a, the left-hand tails of the red line distribution are dominated by the values observed over the oil spill in Fig. 2. It's obvious that the tail is more pronounced at C-band than L-band. Figures 6c and d are the segment results by using the thresholds computed in Figs 6a and b. In the case of C-band, most of the pixels are classified correctly, and the segment result consists of experiment fact. However, in Fig. 6b, the distribution of the polarimetric parameter P value in oil-free area is similar to the oil-covered area. The threshold is set 3.17 at L-band. Moreover, only a few pixels in oil-covered area are recognized as oil spill. Most of the slicks pixels are classified

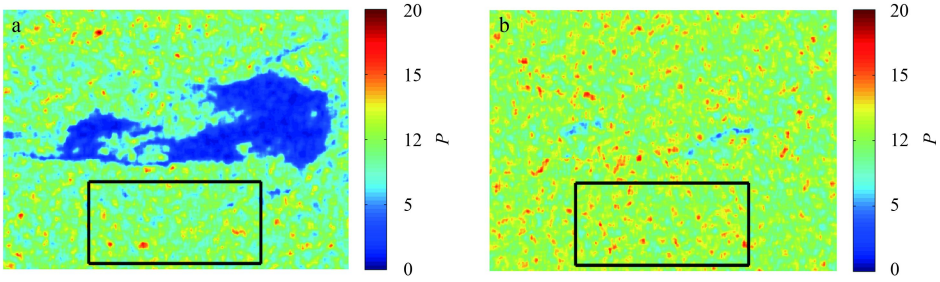

Fig. 5. Polarimetric parameter P extracted from Fig. 2. a. C-band and b. L-band.

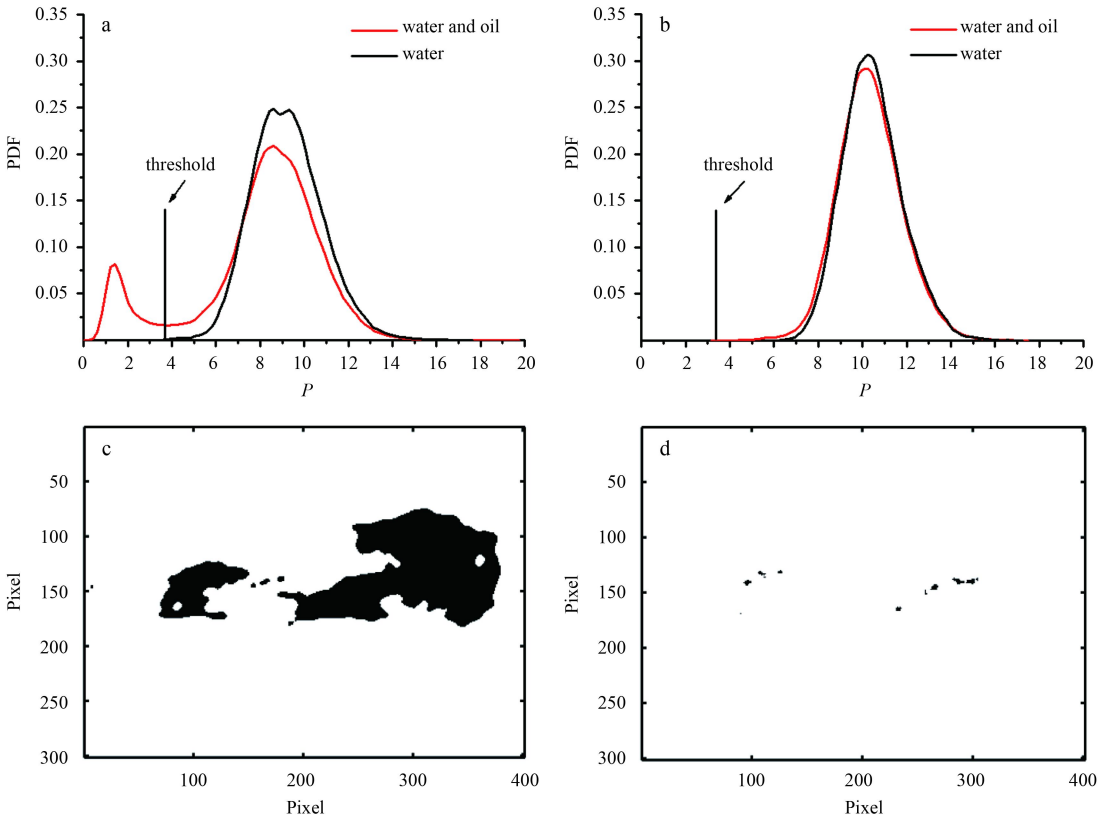

Fig. 6. Histograms of poalrimetric parameter P at C-band (a) and L-band (b), from selected spots on sea water (black lines) and over the entire images (red lines). The histograms were normalized relative to the maximum frequency of occurrence. The segment results correspond to C-band (c) and L-band (d), the thresholds are set to be 3.82 and 3.17, respectively.

as sea water. By the above experiments, one can see that L-band is inferior to C-band, and the parameter P is useful to distinguish the oil spills at C-band.

Knowing from the above experiment, that the C-band SAR performs much better than L-band. However, in some other papers, such as Minchew et al. (2012), the L-band full polarization SAR can separate the oil spills from the sea background clearly. While the L-band SAR data used in this paper cannot distinguish slicks from clean sea as good as Minchew et al. (2012). The discrimination results may be affected by the kinds of slicks, the thickness of slicks, the noise floor or some other external factors. The data used in this paper and in Minchew et al. (2012) have many different factors. The three images used in this paper are collected under similar sea conditions, we suppose that the physical properties and the chemical properties of films influence the discrimination results. Unfortunately, this assumption cannot be assured because we could not get the details about the oil slicks. Further studies are needed to clarify this question. Nevertheless, we can still come to the conclusion that the C-band polarimetric SAR performs better than L-band because the data at two bands used in this paper are acquired under the same condition.

3.3 *Comparison of different polarimetric features at C-band*

In this part, we conduct an experiment for further investigation of different features at C-band. The data used in this part include C-band SIR-C/X SAR data listed in Table 1, and three single look complex (SLC) fine quad-pol C-band SAR images acquired by Radarsat-2. Figure 7a shows a vv polarization Radarsat-2 image collected from the Gulf of Mexico at 12:01 UTC on 8 May 2010. The dark areas are the oil spills which are caused by nature seeps. The incidence angle varies from 41.9° to 43.4°. The wind speed U_{10} is about 6.5 m/s. Figure 7b shows an images acquired during the DWH accidence, at 11:56 UTC on 15 May 2010. The accidence caused larger areas of the oil spills on the sea surface. The oil patches on the right are processed in this experiment. For these data, the incidence angle at near range is 29.2° and the incidence angle at far range is 30.9°. The wind speed U_{10} is 4–7 m/s during the SAR observation. Figure 7c was acquired during the oil spill experiment conducted by the Norway clean seas Association for Operating Companies (NOFO) in the North Sea. Three dark areas can be observed in this image, which correspond to plant oil, oil emulsion and crude oil. In this paper, only the crude oil (right most) is used to investigate the polarimetric features. The wind speed is about 1.6–3.3 m/s when the data is collected (Li et al., 2015). More information about three Radarsat-2 images can be seen in Table 2.

Using the six C-band full polarimetric SAR images, the eight features mentioned above are investigated for the oil spill discrimination. First, the slicks were identified by the visual inspection in the three images. And then the slick-to-sea water contrast of the slicks and sea water is computed on account of the segment results. The slick-to-sea water contrast (Peli, 1990) of different features can be defined as

$$C_{\mathrm{ow}} = \left| \frac{F_{\mathrm{oi}} - F_{\mathrm{wa}}}{F_{\mathrm{oi}} + F_{\mathrm{wa}}} \right|, \tag{30}$$

where F_{oi} the mean value of oil spill regions, and F_{wa} the mean value of sea water. A large value of C_{ow} indicates that the oil spill may be easily separated from water. Figure 8 presents the contrast between the slick and the clean sea water for the eight fea-

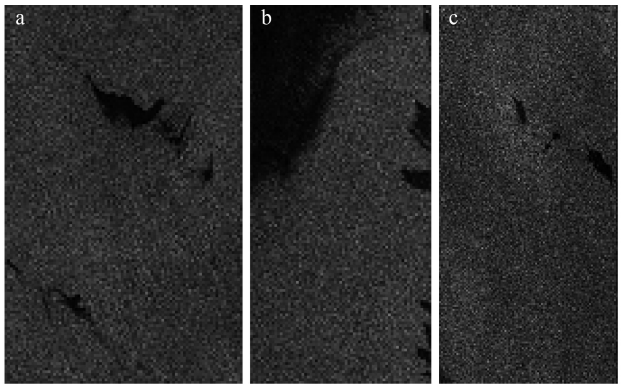

Fig. 7. Intensity images of vv polarized channel. a. RS-1, the dark areas related to the oil slick; b. RS-2, the dark patches were observed during the DWH oil spill event; and c. RS-3, the three dark areas correspond to the plant oil, the oil emulsion and the crude oil from the left to the right, respectively. In this paper, only the crude oil (right most) is used to investigate the polarimetric features.

Table 2. Radarsat-2 data set

Data set	Type and band	Time of acquisition	U_{10}/m·s^{-1}	Incidence angle /(°)
RS-1	fine quad-pol C-band	2010–05–08 12:01	6.5	41.9–43.4
RS-2	fine quad-pol C-band	2010–05–15 11:56	4.0–7.0	29.2–30.9
RS-3	fine quad-pol C-band	2011–06–08 17:27	1.6–3.3	34.5–36.1

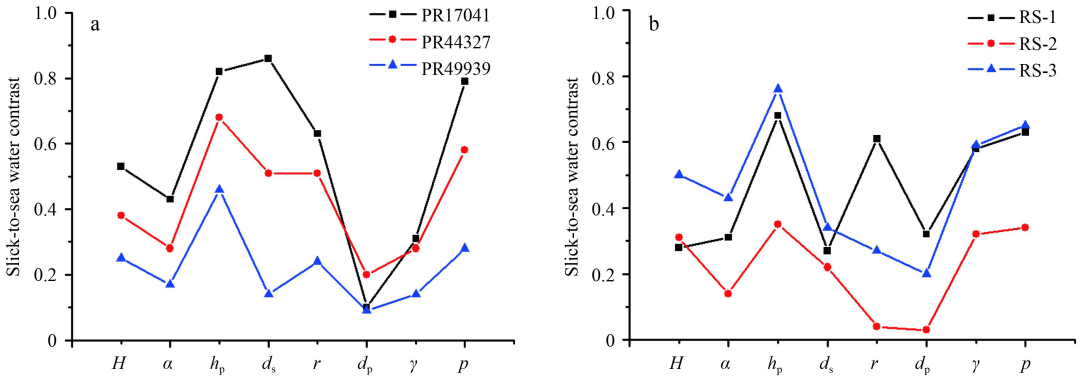

Fig. 8. Contrasts of different polarimetric features between slick and sea water at C-band. a. The features evaluated by the SIR-C\X-SAR data listed in Table 1 and b. the features evaluated by the Radarsat-2 data listed in Table 2.

tures.

In Fig. 8a, the slick-to-sea water contrasts are evaluated based on the three images listed in Table 1, the processing numbers of the three images are PR17041, PR44327, and PR49939, respectively. For data PR17041, the slick-to-sea water contrasts of the pedestal height (0.82), the standard deviation (0.86) of the co-polarized phase difference and P (0.79) are larger than other features. For data PR44327, pedestal height (0.68) and the polarimetric parameter P (0.58) have the larger slick-to-sea water contrasts. While for data PR49939, the polarimetric entropy (0.27), the pedestal height (0.46) and the polarimetric parameter P (0.28) have larger slick-to-sea water contrast C_{ow} values. In Fig. 8b, the slick-to-sea water contrasts are evaluated based on the three images listed in Table 2, the three lines correspond to RS-1, RS-2, RS-3, respectively. For data RS-1, the pedestal height (0.68) and the polarimetric parameter P (0.63) have larger slick-to-sea water contrasts than other features. For data RS-2, pedestal height (0.35) and the polarimetric parameter P (0.34) have larger slick-to-water contrasts. For data RS-3, the pedestal height (0.76) and the polarimetric parameter P (0.65) have larger slick-to-sea water contrasts. Overall, pedestal height and the polarimetric parameter P seem to have the best potential for the oil spill versus the sea water discrimination.

From Fig. 8a, one can see that the variation trend of the three lines are similar to each other. Some parameters will exhibit a different slick-to-sea water contrast in different images. Take polarimetric entropy as an example, the value of slick-to-sea water contrast is 0.53 (PR17041), 0.38 (PR44327) and 0.25 (PR49939), respectively. On the other hand, some parameters exhibit similar values in different data. For instance, the slick-to-sea water contrast of d_p in PR17041 (0.1) and PR49939 (0.09) are almost same. It seems that the value of the slick-to-sea water contrast will affected by the thickness of films, the wind speed and some other environmental factors. Unfortunately, we are not sure which factor is most important. Further studies are needed to explain this phenomenon.

4 Conclusions

In recent years, with the advance of SAR technology, polarimetric SAR has been used to monitor oil spill accidents on the sea surface. The full-polarized SAR could collect more information of oil spill than single polarized SAR. In this work, we study

seven common polarimetric features and propose a new parameter defined as the polarimetric parameter *P*. The capability of the polarimetric features for a sea oil spill observation is investigated. First, we compare C-band with L-band based on the SIR-C/X-SAR data, the experiment results show that the polarimetric features in the C-band SAR images are sensitive to the sea surface scattering mechanisms. Meanwhile, the slick-to-sea water contrasts of the eight features are also compared with each other in C-band SIR-C/X-SAR and Radarsat-2 images.

In summary, according to the above experiment results, under low to moderate conditions, the key conclusions can be summarized as follows:

(1) C-band performs better than L-band for the oil spill detection.

(2) The new polarimetric parameter *P* is sensitive to the sea surface scattering mechanisms at C-band.

(3) Among the features which are used to detect the oil spills, the pedestal height and the new parameter *P* perform better than other features.

The paper introduces a basic research for the oil spill discrimination with the polarimetric SAR. The polarimetric features can be utilized for the discrimination between the oil spill and the look-alike phenomenon in further research.

Acknowledgements

The authors thank the NASA Jet Propulsion Laboratory for providing the SIR-C/X-SAR data used in this study.

References

Brekke C, Solberg A H S. 2005. Oil spill detection by satellite remote sensing. Remote Sens Environ, 95(1): 1–13

Cloude S R, Pottier E. 1996. A review of target decomposition theorems in radar polarimetry. IEEE Trans Geosci Remote Sens, 34(2): 498–518

Durden S L, Van Zyl J J, Zebker H A. 1990. The unpolarized component in polarimetric radar observations of forested areas. IEEE Trans Geosci Remote Sens, 28(2): 268–271

Fiscella B, Giancaspro A, Nirchio F, et al. 2000. Oil spill detection using marine SAR images. Int J Remote Sens, 21(18): 3561–3566

Lee J S, Pottier E. 2009. Polarimetric Radar Imaging: from Basics to Applications. Boca Raton: CRC Press

Li Haiyan, Perrie W, He Yijun, et al. 2015. Analysis of the polarimetric SAR scattering properties of oil-covered waters. IEEE J Sel Top Appl Earth Obs Remote Sens, 8(8): 3751–3759

Lombardini P P, Fiscella B, Trivero P, et al. 1989. Modulation of the spectra of short gravity waves by sea surface films: slick detection and characterization with a microwave probe. J Atmos Oceanic Technol, 6(6): 882–890

Migliaccio M, Nunziata F, Buono A. 2015. SAR polarimetry for sea oil slick observation. Int J Remote Sens, 36(12): 3243–3273

Migliaccio M, Nunziata F, Gambardella A. 2009. On the co-polarized phase difference for oil spill observation. Int J Remote Sens, 30(6): 1587–1602

Migliaccio M, Tranfaglia M. 2005. A study on the capability of sar polarimetry to observe oil spills. ESA Special Publication, 586: 25–30

Minchew B, Jones C E, Holt B. 2012. Polarimetric analysis of backscatter from the Deepwater Horizon oil spill using L-band synthetic aperture radar. IEEE Trans Geosci Remote Sens, 50(10): 3812–3830

Nunziata F, Gambardella A, Migliaccio M. 2013. On the degree of polarization for SAR sea oil slick observation. ISPRS J Photogramm Remote Sens, 78: 41–49

Nunziata F, Migliaccio M, Gambardella A. 2011. Pedestal height for sea oil slick observation. IET Radar, Sonar Navig, 5(2): 103–110

Peli E. 1990. Contrast in complex images. J Opt Soc Am A, 7(10): 2032–2040

Pinel N, Dechamps N, Bourlier C. 2008. Modeling of the bistatic electromagnetic scattering from sea surfaces covered in oil for microwave applications. IEEE Trans Geosci Remote Sens, 46(2): 385–392

Salberg A B, Rudjord O, Solberg A H S. 2012. Model based oil spill detection using polarimetric SAR. In: Proceedings of 2012 IEEE International Geoscience and Remote Sensing Symposium. Munich: IEEE, 5884–5887

Salberg A B, Rudjord O, Solberg A H S. 2014. Oil spill detection in hybrid-polarimetric SAR images. IEEE Trans Geosci Remote Sens, 52(10): 6521–6533

Schuler D L, Lee J S. 2006. Mapping ocean surface features using biogenic slick-fields and SAR polarimetric decomposition techniques. IEE Proc Radar, Sonar Navig, 153(3): 260–270

Schuler D L, Lee J S, Hoppel K W. 1993. Polarimetric SAR image signatures of the ocean and Gulf Stream features. IEEE Trans Geosci Remote Sens, 31(6): 1210–1221

Skrunes S, Brekke C, Eltoft T. 2012. Oil spill characterization with multi-polarization C-and X-band SAR. In: Proceedings of 2012 IEEE International Geoscience and Remote Sensing Symposium. Munich: IEEE, 5117–5120

Skrunes S, Brekke C, Eltoft T. 2014. Characterization of marine surface slicks by Radarsat-2 multipolarization features. IEEE Trans Geosci Remote Sens, 52(9): 5302–5319

Solberg A H S, Brekke C, Ove Husoy P. 2007. Oil spill detection in radarsat and envisat SAR images. IEEE Trans Geosci Remote Sens, 45(3): 746–755

Velotto D, Migliaccio M, Nunziata F, et al. 2011. Dual-polarized TerraSAR-X data for oil-spill observation. IEEE Trans Geosci Remote Sens, 49(12): 4751–4762

Zhang Biao, Perrie W, Li Xiaofeng, et al. 2011. Mapping sea surface oil slicks using RADARSAT-2 quad-polarization SAR image. Geophys Res Lett, 38(10): L10602